Neutron density distributions of ^{204,206,208}Pb deduced via proton elastic scattering at $E_p = 295$ MeV

J. Zenihiro,[1,*] H. Sakaguchi,[1,†] T. Murakami,[1] M. Yosoi,[1,†] Y. Yasuda,[1,†] S. Terashima,[1,‡] Y. Iwao,[1] H. Takeda,[2] M. Itoh,[3,§] H. P. Yoshida,[3,§] and M. Uchida[3,‖]

[1]*Department of Physics, Kyoto University, Kyoto 606-8502, Japan*

[2]*RIKEN Nishina Center for Accelerator-Based Science, Wako, Saitama 351-0198, Japan*

[3]*Research Center for Nuclear Physics, Osaka University, Ibaraki, Osaka 567-0047, Japan*

(Received 12 September 2010; published 22 October 2010)

Cross sections and analyzing powers for polarized proton elastic scattering from ^{58}Ni, and ^{204,206,208}Pb were measured at intermediate energy $E_p = 295$ MeV. An effective relativistic Love-Franey interaction is tuned to reproduce ^{58}Ni scattering data within the framework of the relativistic impulse approximation. The neutron densities of the lead isotopes are deduced using model-independent sum-of-Gaussians distributions. Their error envelopes are estimated by a new χ^2 criterion including uncertainties associated with the reaction model. The systematic behaviors of extracted error envelopes of the neutron density distributions in ^{204,206,208}Pb are presented. The extracted neutron and proton density distribution of ^{208}Pb gives a neutron skin thickness of $\Delta r_{np} = 0.211^{+0.054}_{-0.063}$ fm.

DOI: 10.1103/PhysRevC.82.044611 PACS number(s): 21.10.Gv, 21.65.Ef, 25.40.Cm, 27.80.+w

I. INTRODUCTION

The nucleon density distribution is one of the most fundamental properties of nuclei. For the last few decades, new phenomena such as skin and halo structures have been found from the study of unstable nuclei, whose neutron number N is very different from its proton number Z. The precise extraction of the nucleon density distribution is very important in studying these phenomena.

Heavy nuclei are also expected to have a neutron skin structure. Both relativistic and nonrelativistic mean-field models suggest that the thickness of the neutron skin (Δr_{np}), defined as the difference between the neutron (r_n) and proton (r_p) root-mean-square (rms) radii ($\Delta r_{np} \equiv r_n - r_p$), depends on the balance among the various nuclear matter properties. In particular, the neutron skin thickness of ^{208}Pb is strongly correlated with the nuclear symmetry energy or the pressure coefficients of the equation of states (EOS) in neutron matter [1–3]. Moreover, it was suggested that a precise measurement of the skin thickness of ^{208}Pb is very important for studying the radius, composition, and cooling system of neutron stars [4,5].

In the case of stable nuclei, the proton density and radius can be derived from the nuclear charge. Charge distributions for a variety of stable nuclei are now known accurately from a large number of experiments [6,7]. For example, the charge radius of ^{208}Pb is 5.5010(9) fm with an accuracy of 0.02% according to a combined analysis of electron scattering, muonic atom x rays, and isotope shift as shown in Ref. [7]. An electromagnetic probe, due to its simple reaction mechanism, can extract precise information about charge density deep inside a nucleus.

Neutron density and radius were studied by many researchers using proton, α, pion scattering, and antiprotonic atoms [8–19]. However, typical uncertainties of extracted neutron rms radius are more than ten times as large as those of the charge radius. Hadronic probes exhibit uncertainties in the reaction mechanism, which is mainly caused by an incomplete knowledge of the nucleon-nucleon (NN) scattering amplitude inside the nuclear medium. To extract precise information about the neutron density distribution an appropriate probe and an effective NN interaction must be carefully chosen.

Proton-nucleus elastic scattering at intermediate energies ($E_p \sim 300$ MeV) is a relatively good probe for extracting information about both the nuclear surface and interior. The energy of the incident protons is low enough to suppress meson production and hence allow a shallow absorptive potential to be obtained. It is also high enough to be described by an impulse approximation. As mentioned previously, however, uncertainties in the NN interaction in the nucleus are a problem. In previous articles [20,21], we reduced the uncertainties in the NN interaction inside the nuclear medium by introducing a phenomenological medium modification in the relativistic Love-Franey interaction in terms of the density-dependent parameters. This correction is effectively described as a modification of the masses and coupling constants of the exchanged mesons according to the nucleon density. To calibrate these "medium effect" parameters, we use proton elastic scattering from ^{58}Ni because the proton and neutron densities are supposed to have almost the same shape and radius in ^{58}Ni [9,17,22,23]. Then, using the medium-effect parameters calibrated for ^{58}Ni, we extracted the neutron density distributions of tin isotopes in the form of model-independent sum-of-Gaussians (SOG) distributions. The accuracy of the neutron radii of tin isotopes were found to be less than 0.03 fm including both the statistical and model uncertainties [21].

*juzo@rcnp.osaka-u.ac.jp; Present address: Research Center for Nuclear Physics, Osaka University, Ibaraki, Osaka 567-0047, Japan.

†Present address: Research Center for Nuclear Physics, Osaka University, Ibaraki, Osaka 567-0047, Japan.

‡Present address: Department KPII, GSI Helmholtzzentrum fur Schwerionenforschung GmbH Planckstrasse 1, D-64291 Darmstadt, Germany.

§Present address: Cyclotron and Radioisotope Center, Tohoku University, Sendai, Miyagi, 980-8578, Japan.

‖Present address: Department of Physics, Tokyo Institute of Technology, Meguro, Tokyo 152-8551, Japan.

The purpose of this work is to evaluate the sensitivity of proton elastic scattering to the neutron densities in heavy nuclei such as lead isotopes. We focus on the extracted neutron skin thickness of ^{208}Pb. There have been several attempts to extract the neutron density distributions of ^{208}Pb from proton elastic scattering data [9,13]. The energy of the incident protons, $E_p = 650$ and 800 MeV used in Refs. [9,13], are rather high, where the real part of the optical potential is completely repulsive and the imaginary part is about 50 MeV deep. Thus the information about the nuclear interior is masked by the strong absorption. To avoid this large ambiguity of the interior structure, Starodubsky and Hintz [13] assumed that the nuclear matter density in the nuclear interior is almost constant. They did not use the model-independent function itself to extract the neutron density, but instead used the Skyrme-Hartree-Fock density plus a small correction expanded in a Fourier-Bessel series to estimate the error envelopes of the neutron densities, which reflect only the statistical errors of the experimental data. They also used a density-dependent t matrix calibrated by p-^{40}Ca scattering data in the framework of the nonrelativistic formalism. Their approach is very similar to ours, as seen in our previous study for tin isotopes [21], but they did not estimate the errors due to the model ambiguity, which is an unavoidable problem in describing hadronic reactions.

There are several theoretical approaches for energy-independent global analysis. Skyrme-Hartree-Fock models with modern parametrizations were tested employing the g-folding optical potential to explain the data obtained from nucleon-nucleus elastic scattering from ^{208}Pb at 40, 65, and 200 MeV [14]. It was suggested that ^{208}Pb has a neutron skin thickness of $\sim$0.17 fm because the SkM* model gives the best agreement with the experimental data. Another global analysis of proton-nucleus elastic scattering data in the energy range from 500 to 1040 MeV based on the Dirac phenomenological optical model in Ref. [15] gave a range of Δr_{np} from 0.083 to 0.111 fm for ^{208}Pb. The obtained range of Δr_{np} changes depending on the momentum transfer range and the NN interaction used for the global fit. In these theoretical approaches, statistical errors and the effect of the model dependence must be considered in the error estimation of Δr_{np}.

As a different experimental approach, a parity-violating electron elastic scattering measurement to extract the neutron radius in ^{208}Pb (PREX) was proposed at Jefferson Laboratory [24–26]. This challenging experiment is planned to measure the model-independent neutron rms radius for ^{208}Pb with an accuracy of 1% assuming a simple model-dependent function such as a Woods-Saxon for the nuetron density of ^{208}Pb. The advantage of this method is its model independence, but the planned accuracy is larger than the recent measurements using hadronic probes [13,18,19].

In this article we report our results of quantifying the uncertainty of both the experimental data and the present reaction model as the errors of the neutron densities in lead isotopes. The experimental data of proton elastic scattering from ^{58}Ni, and ^{204,206,208}Pb at $E_p = 295$ MeV are newly obtained and several improvements are applied, as explained in Sec. II, so as to reduce the systematic uncertainties which have not been considered previously. This work is mainly based on the approach and technique described in Refs. [20,21]. A brief outline of the medium-modified relativistic impulse approximation (RIA) model and the results of the extraction of the neutron density distributions in lead isotopes are given in Sec. III. We provide a summary in Sec. IV.

II. EXPERIMENTAL PROCEDURE

The experiment was performed at the Research Center for Nuclear Physics (RCNP), Osaka University. Polarized protons produced by a high-intensity polarized ion source (HIPIS) [27] were injected into an azimuthally varying field (AVF) cyclotron to keep the polarization axis in the vertical direction. The polarized proton beam at 53 MeV from the AVF cyclotron was further accelerated to 295 MeV using the six-sector ring cyclotron in a coupled mode. The spin direction and the polarization of the beam were constantly monitored during the measurement with a sampling-type beam line polarimeter (BLP) placed before a scattering chamber. To determine the vertical components p_y of the polarization, the BLP used left-right asymmetries in p-H scattering from a $(CH_2)_n$ foil [28]. A typical beam polarization was about 70%. The beam extracted from the ring cyclotron was achromatically transported to a target in a scattering chamber. A typical size of the beam spot was 1 mm in diameter. In the measurement at forward angles, the proton beam was stopped in a Faraday cup placed inside the scattering chamber (SCFC). In the measurement at backward angles the proton beam was stopped in another Faraday cup located about 25 m downstream from the scattering chamber (WallFC). The beam current was monitored using a current integrator (Model 1000C, Brookhaven Instruments Corporation). The relative charge collection efficiencies between the SCFC and WallFC were monitored using the p-H cross sections at the BLP during the measurement. The beam current on the target was altered between 5 and 380 nA to keep the dead time of the data acquisition less than 10%.

Targets consisting of, respectively, foils of three lead isotopes (^{204,206,208}Pb) and ^{58}Ni were used, as shown in Table I. Two types of targets of ^{206,208}Pb and ^{58}Ni, namely thin and thick ones, were used for the measurements at forward and backward angles, respectively. To reduce the relative systematic errors due to instabilities of the beam conditions or detectors, the four targets were automatically interchanged every $\sim$5 minutes at each scattering angle. The beam condition itself was constantly checked using the BLP data. Beam viewers placed at the target position and a momentum-dispersive position before the scattering

TABLE I. Target thicknesses and enrichments of Ni and lead isotopes.

Nucleus	Thin	Thick	Enrichment
^{204}Pb	23.7 mg/cm^2	not prepared	99.6%
^{206}Pb	18.4 mg/cm^2	50.9 mg/cm^2	99.3%
^{208}Pb	31.5 mg/cm^2	78.8 mg/cm^2	99.7%
^{58}Ni	39.5 mg/cm^2	100 mg/cm^2	99.39%

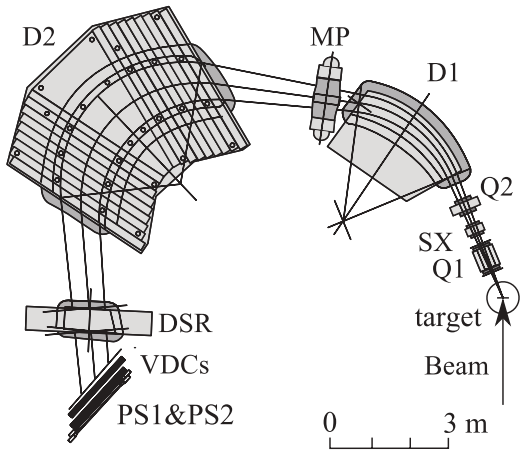

FIG. 1. Schematic view of the spectrometer "Grand Raiden" and the focal plane detectors.

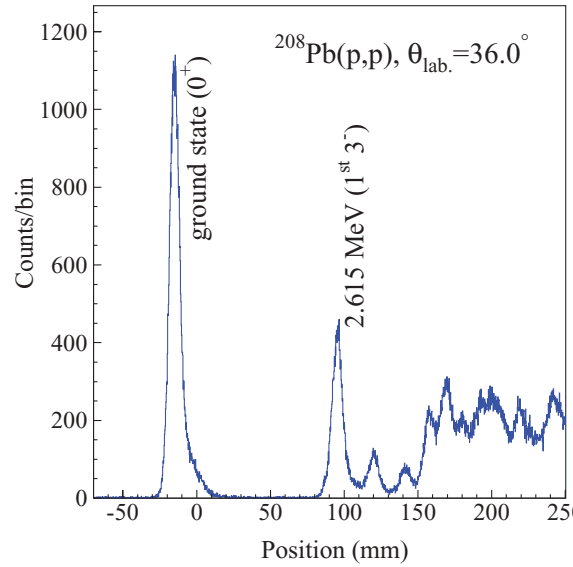

FIG. 2. (Color online) Typical position spectrum at the focal plane for ^{208}Pb at a laboratory angle of 36.0°.

chamber were also used to check the beam condition after each run. The uncertainty of the scattering angle was less than ±0.05°.

Scattered protons were analyzed using the QSQDMD-type high resolution magnetic spectrometer, "Grand Raiden" (Q: quadrupole; S: sextupole; D: dipole; M: multipole) [29]. The trajectories of the scattered protons were determined with two sets (X, U and X′, U′) of vertical-type drift chambers (VDC's), placed at the focal plane of Grand Raiden. Two 1-cm-thick plastic scintillators (PS1 and PS2) right behind the VDC's were used to generate the start signal of the data acquisition. A 1-cm-thick aluminum plate was placed between the two plastic scintillators to prevent δ electrons knocked out by scattered particles at PS1 from entering PS2. A schematic view of Grand Raiden and the focal-plane detectors is shown in Fig. 1.

Protons were identified by using the information about both the time of flight and the energy loss (ΔE) in PS1 and PS2. In the previous analysis only the information about ΔE was used for particle identification [20,21]. The proton peak in the ΔE spectrum has a tail structure and the proton events in the tail were cutoff together with the deuteron and triton events. This causes the reduction of the yields, which accounts for more than a few percent of the total and is not negligible for the precise measurement of the cross sections.

Moreover, to reconstruct the trajectories of scattered particles from the VDC data, we applied the multicluster treatment reported in Ref. [30]. This treatment is effective for avoiding the severe reduction of the yields and efficiencies of a VDC especially at the angles where the signal-to-noise ratios are small. The energy resolution during the measurement was better than 200 keV in full width at half maximum. A typical position spectrum of ^{208}Pb at the focal plane is shown in Fig. 2.

The absolute charge-collection efficiency of the SCFC and the absolute trigger efficiency of PS1 and PS2 for protons at 295 MeV were recently measured in a separate experiment [31]. A well-calibrated Faraday cup and triple coincidence of three consecutive scintillators were arranged as references to these efficiencies. In the present analysis, these efficiencies are taken into account.

As a result of these improvements, the new data set of cross sections for ^{58}Ni is about 10% larger than the previous set used in Refs. [20,21].

Data sets of angular distributions of differential cross sections and analyzing powers for polarized proton elastic scattering from ^{58}Ni and ^{204,206,208}Pb were obtained over an angular range of $7^\circ < \theta < 50^\circ$, corresponding to a range of momentum transfer from 0.55 to 3.5 fm^{-1}.

III. RESULTS AND DISCUSSION

A. Relativistic impulse approximation

The details of our approach are described in Refs. [20,21] and only a brief description of the method to extract the neutron density distributions is given in this article.

The analysis method is based on the framework of the RIA using the relativistic Love-Franey (RLF) NN interaction proposed by Murdock and Horowitz (MH model) [32]. In the MH model the nucleon-nucleus optical potential is calculated by folding the RLF NN interaction with the nucleon vector and scalar density of the target nucleus. Figure 3 shows the obtained experimental data of cross sections and analyzing powers for elastic scattering from ^{204,206,208}Pb and ^{58}Ni compared with two kinds of model calculations. The solid and dashed lines are the RIA calculations [32] with Dirac-Hartree (DH) [34] densities of the target nuclei and the calculations using the recent global Dirac optical model by Cooper, Hama, and Clark [33], respectively. Although both calculations well reproduce the analyzing powers, only the global Dirac optical model is in good agreement with the cross sections. The MH model poorly reproduces the angular distributions of the cross section especially at backward angles. This is because neither the RLF interaction nor the nucleon densities used in the MH model are realistic. However, even though a realistic nucleon density of ^{58}Ni, as mentioned later, was used in place of the DH density for the MH calculation (dash-dotted lines in Fig. 3), the

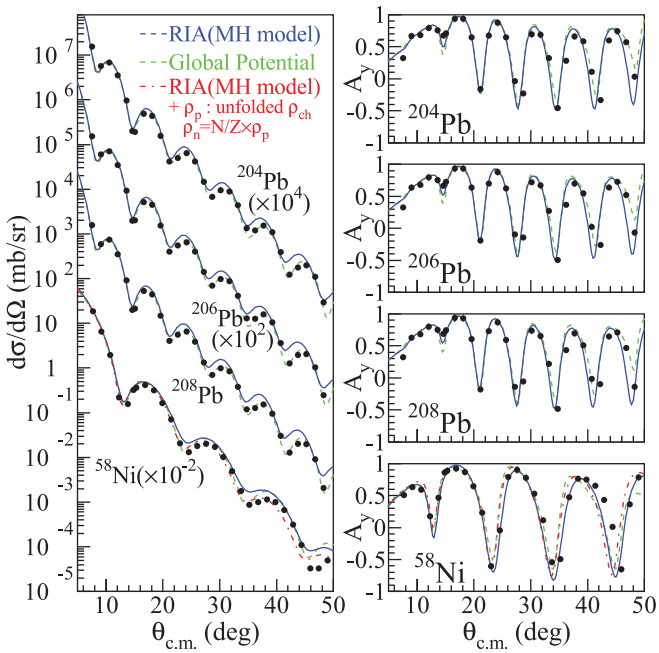

FIG. 3. (Color online) Obtained data of differential cross sections and analyzing powers for elastic scattering from ^{58}Ni and ^{204,206,208}Pb at $E_p = 295$ MeV, whereas the lines are due to Murdock and Horowitz (solid) [32] and the global Dirac optical potential (dashed) [33]. The dash-dotted lines show the MH model calculations for ^{58}Ni with the realistic nucleon density by an unfolding charge density.

disagreement with the experimental data of ^{58}Ni still remains. To explain the experimental data we need the effective NN interaction inside the nuclear medium in place of the RLF interaction.

A realistic point proton density distribution was determined by unfolding the nuclear charge distribution extracted from electron elastic scattering [6,35] with the intrinsic charge distributions of the proton and neutron. Using the Fourier transform of the radial density $\tilde{\rho}(q) = \mathcal{F}\{\rho(r)\}$ where q is the momentum transfer, the relationship between the charge, proton, neutron, intrinsic proton-charge, and intrinsic neutron-charge densities ρ_{ch}, ρ_p, ρ_n, ρ^p_{ch}, ρ^n_{ch} is approximately described as

$$\begin{aligned}\tilde{\rho}_{ch}(q) &\simeq \tilde{\rho}_p(q)\tilde{\rho}^p_{ch}(q) + \tilde{\rho}_n(q)\tilde{\rho}^n_{ch}(q) \\ &\simeq \tilde{\rho}_p(q)G^p_E(q^2) + \tilde{\rho}_n(q)G^n_E(q^2),\end{aligned} \tag{1}$$

where, in the nonrelativistic limit, $\tilde{\rho}^{p(n)}_{ch} \simeq G^{p(n)}_E(q^2)$ is the experimentally determined Sachs electric form factor in a proton (neutron). The correction term by the spin-orbit and relativistic effects on the Sachs form factors in the Breit frame, the so-called Darwin-Foldy correction, are negligible because their effects on the nuclear size are one order smaller than the neutron-charge radius and comparable with the error of a charge radius as shown in Refs. [9,36].

For the intrinsic nucleon charge form factor $\tilde{\rho}^{p(n)}_{ch}$, we adopted a new set of nucleon electromagnetic form factors which were recently extracted from the re-analysis of the *world e-p* and *e-d* scattering data at low-momentum transfers from 0.3 to 1 GeV^2/c^2 where the nucleon charge form factor is very sensitive to its model-independent charge radius [37,38]. The proton-charge radius of 0.895(18) fm obtained from $\tilde{\rho}^p_{ch}$ in Refs. [37,38] is much larger than the value of 0.863(4) fm used in the previous work [39], but is consistent with the value of 0.883(14) fm obtained from the recent measurement of the hydrogen $1S$ Lamb shift [40].

In the case of ^{58}Ni, the neutron rms radius is expected to be almost the same as the proton rms radius. Therefore we assumed that the neutron density of ^{58}Ni has the same shape as the proton density, that is, $\rho_n = (N/Z)\rho_p$.

For the RIA calculations, scalar density distributions are necessary as well as baryon density distributions. Scalar density distributions cannot be extracted directly, unless the wave functions of the ground state are known in advance. According to the DH calculations for heavy nuclei, the ratios between the scalar and vector densities S/V are almost constant at 0.96, as reported in Refs. [20,21]. Therefore, we simply assumed a scalar density ρ^S of $\rho^S = 0.96\rho^V$ for a vector density ρ^V using the realistic nucleon density.

B. Medium-modified RIA

The RLF interaction in the MH model is described by a set of five Lorentz covariant functions and was determined from the free NN phase shift analysis. It was found that the free NN interaction cannot fully reproduce the experimental data at high-momentum transfers even using the realistic nucleon density. To explain the experimental data, we introduced a medium modification into the RLF NN scattering amplitudes by varying the coupling constants and masses of the σ and ω mesons depending on the local density as follows:

$$g_j^2,\ \bar{g}_j^2 \to \frac{g_j^2}{1 + a_j\rho(r)/\rho_0},\ \frac{\bar{g}_j^2}{1 + \bar{a}_j\rho(r)/\rho_0} \tag{2}$$

$$m_j,\ \bar{m}_j \to m_j\left[1 + b_j\frac{\rho(r)}{\rho_0}\right],\ \bar{m}_j\left[1 + \bar{b}_j\frac{\rho(r)}{\rho_0}\right] \tag{3}$$

$$j = \sigma, \omega,$$

where $m_j, \bar{m}_j, g_j$, and $\bar{g}_j$ are the masses and coupling constants of σ and ω mesons for real and imaginary amplitudes, respectively. The normal density ρ_0 is 0.1934 fm^{-3}. In free space, where the density of the target nucleus is zero, the masses and coupling constants of the exchanged mesons are set to be the same as those of the free NN interaction, but inside the nucleus the modification is assumed to be proportional to the nucleon density $\rho(r)$ with the phenomenological parameters a_j, $\bar{a}_j$, b_j, and $\bar{b}_j$. This density dependence describes the first-order approximation in terms of the nuclear density and partially explains various many-body effects such as Pauli blocking, multistep processes, and the partial restoration of chiral symmetry. Since the modification has a universal form of local-density dependent terms, we can apply it to any other nuclei once the parameters are calibrated with a real nucleus. At the present stage we used four parameters assuming the same modification for the real and imaginary parts of the NN scattering amplitude ($a_j = \bar{a}_j, b_j = \bar{b}_j$) because with eight

parameters there are so many degrees of freedom that these parameters have strong correlations with each other.

The extraction of the neutron densities of lead isotopes is based on the medium-modified RIA calculation with realistic proton densities. For this purpose we first need to determine the medium-modification of the effective RLF interaction. In the next section, we report the calibration of the medium-effect parameters using the experimental data of proton elastic scattering from ^{58}Ni.

C. Calibration of the effective NN interaction

For the calibration of the four medium-effect parameters, a_j and b_j ($j = \sigma, \omega$), we have chosen p-^{58}Ni elastic scattering because ^{58}Ni is the heaviest spherical nucleus with $N \approx Z$ and the neutron density of ^{58}Ni is expected to have a similar distribution to the proton density [$\rho_n = (N/Z)\rho_p$]. Both the experimental and theoretical results [9,17,22,23] support a neutron rms radius for ^{58}Ni that is almost the same as the proton rms radius, while for $N = Z$ nuclei, such as ^{40}Ca or ^{56}Ni, the proton rms radii are larger than the neutron rms radii due to Coulomb repulsion. The realistic proton density of ^{58}Ni is extracted by unfolding the charge density with the new intrinsic nucleon-charge density.

A fit to the ^{58}Ni data of cross sections and analyzing powers obtained in this experiment and spin rotation parameters previously measured at the same energy [30] was carried out by χ^2 test [41] with the four medium-effect parameters. The value of χ^2 is given by

$$\chi^2 = \sum_{\theta_i} \left(y_{\theta_i}^{\rm exp} - y_{\theta_i}^{\rm calc}\right)^2 / \Delta y_{\theta_i}^2, \qquad (4)$$

where $y_{\theta_i}^{\rm exp}$, Δy_{θ_i}, and $y_{\theta_i}^{\rm calc}$ are the ith experimental data, error, and medium-modified RIA calculation for ^{58}Ni at each θ_i. The best-fit parameters providing a minimum of χ^2 ($\chi^2_{\rm min}$) are listed in Table II. The solid line in Fig. 4 is the medium-modified RIA calculation with these best-fit parameters and the realistic nucleon densities deduced from the charge distribution. Compared to the previous work [21], the modifications by the best-fit parameters are very small. The best-fit calculations are in better agreement with the experimental data than the previous data even though the number and angular range of the data points is much larger than for the previous data [20,21]. This means that the improvements to reduce the experimental systematic uncertainties work very well. The standard error of each best-fit parameter in Table II was determined from a contour corresponding to an increase of 1 in χ^2 from $\chi^2_{\rm min}$ by allowing all the other parameters to vary freely to minimize χ^2 for each chosen value of the parameter.

TABLE II. Best-fit medium-effect parameters a_j and b_j ($j = \sigma, \omega$) in Eqs. (2) and (3).

j	σ	ω
a_j	-0.044 ± 0.026	0.037 ± 0.040
b_j	0.097 ± 0.013	0.075 ± 0.021

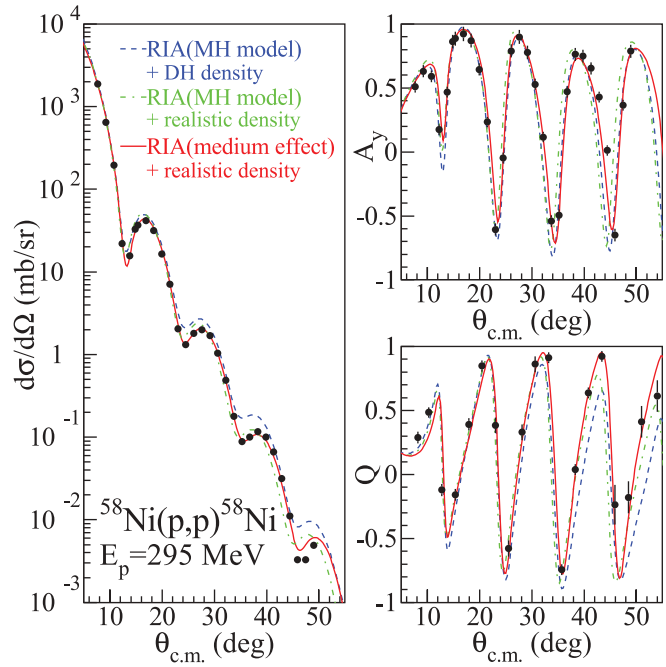

FIG. 4. (Color online) Calibration of medium-effect parameters by fitting to the experimental data for ^{58}Ni. The solid line is the medium-modified RIA calculation with best-fit parameters The dashed and dash-dotted lines are from the original MH model with DH and realistic nucleon densities.

D. Extraction of neutron density distributions

Using the effective NN interaction calibrated by ^{58}Ni data we extracted the neutron density distributions of ^{204,206,208}Pb. The realistic proton density distributions of lead isotopes were also used by unfolding charge distributions.

To find the best-fit neutron density distribution, we used a nSOG function, which has been originally investigated in the model-independent analysis of charge distributions [6,35]. The SOG neutron density is described as

$$\rho_n(r) = \frac{N}{2\pi^{3/2}\gamma^3} \sum_{i=1}^{12} \frac{Q_i}{1 + 2R_i^2/\gamma^2} \times \left(e^{-(r-R_i)^2/\gamma^2} + e^{-(r+R_i)^2/\gamma^2}\right), \qquad (5)$$

where N and Q_i are the number of neutrons, and the fraction of N in the ith Gaussian with the normalization condition $\sum_i Q_i = 1$, respectively. For simplicity we fixed the width γ and position R_i of the ith Gaussian to the same values used for the charge distributions of ^{208}Pb in Ref. [6] since the e-^{208}Pb elastic scattering data covers a wider range of momentum transfer from 0.44 to 3.7 fm^{-1} than our data from 0.55 to 3.5 fm^{-1}. We searched for the best-fit values of Q_i by the χ^2 method. Figure 5 shows the results of the medium-modified RIA calculations with the best-fit neutron density distributions of ^{204,206,208}Pb (solid lines). The medium-modified RIA calculations with the DH nucleon density (dash-dotted lines) well reproduce the analyzing powers and the angular positions of the diffraction peaks and minima compared with the original MH calculations (dashed lines), but still overestimate the absolute values of the cross sections.

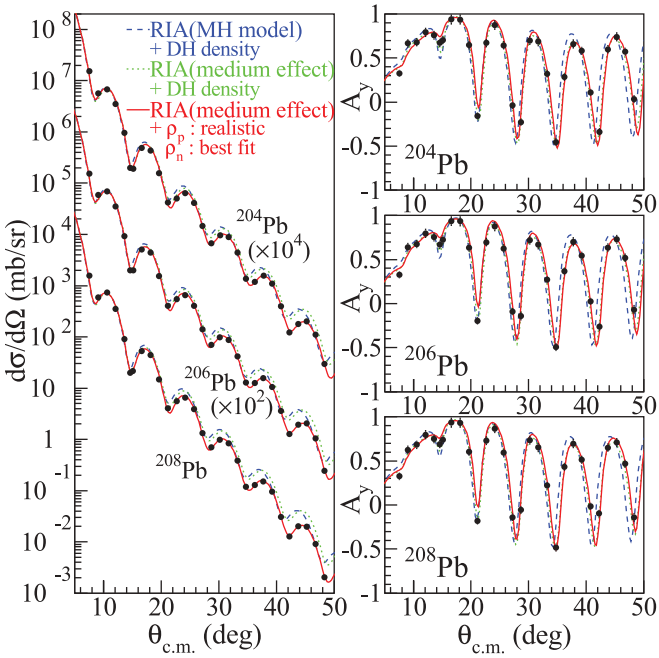

FIG. 5. (Color online) Best-fit results for neutron density distributions in ^{204,206,208}Pb are shown as solid lines. The original MH and medium-modified RIA calculations with the DH nucleon density are also shown by dashed and dash-dotted lines.

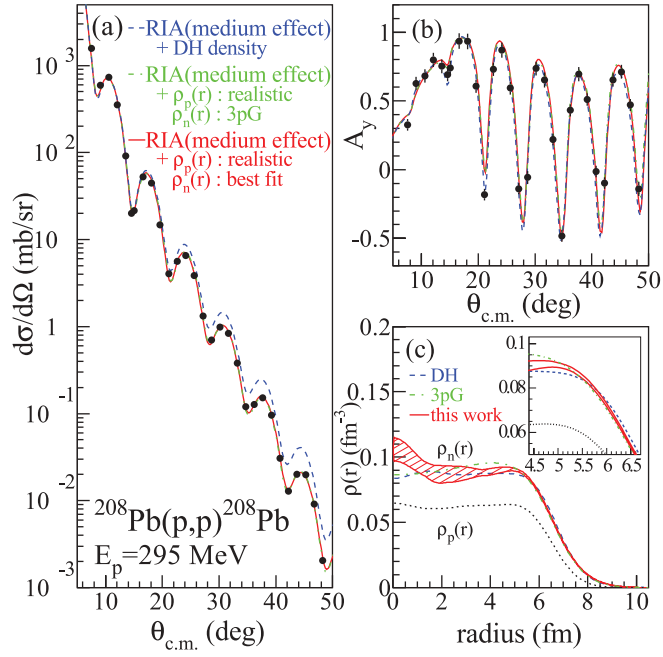

FIG. 6. (Color online) Results of fitting to the experimental data and extracted neutron density of ^{208}Pb with its standard error envelope (solid lines). The dashed and dash-dotted lines are medium-modified RIA calculations, but using the DH nucleon densities and the 3pG neutron density by Ray [9], respectively.

The best-fit calculations (solid lines) are in good agreement with the experimental data of both the cross sections and analyzing powers even in the high-momentum transfer region up to 3.5 fm^{-1}. The nucleon density distributions are found to affect the absolute values of the cross sections quite directly. The typical reduced $\chi^2_{\rm min}$, namely $\chi^2_{\rm min}/\nu$, where ν is the number of degrees of freedom, is about 4.

The standard error envelopes of the neutron density distributions due to the experimental errors can be estimated by the increase $\Delta\chi^2$ corresponding to 1 standard deviation from $\chi^2_{\rm min}$, expressed as the following inequality:

$$\chi^2 \leqslant \chi^2_{\rm min} + \Delta\chi^2. \tag{6}$$

For the error estimation of the neutron density we need to know theone standard deviation region encompassed by the joint variation of multiparameters. $\Delta\chi^2$ for multiparameters obeys the χ^2 probability distribution function for m degrees of freedom, where m is the number of fitted parameters [41] and is roughly equal to m for 1 standard deviation ($\Delta\chi^2 \approx m = 11$ in this case). By using the Monte Carlo technique, we determined both the minimum and maximum envelopes of all the possible neutron density distributions that satisfy Eq. (6) as the standard error envelope. The errors of the neutron rms radii are also determined from the maximum and minimum value of the rms radii of the allowed neutron density distributions.

Figure 6 shows the case of ^{208}Pb. The hatched area surrounded by the solid lines in Fig. 6(c) shows the standard error envelope of the neutron density in ^{208}Pb estimated by Eq. (6), together with the DH neutron density distribution (dashed line). The three-parameter-Gaussian (3pG) neutron density extracted from the p-^{208}Pb elastic scattering at 800 MeV using the second-order Kerman-McManus-Thaler (KMT) model [9] (dash-dotted line) is also shown for comparison. The inset in Fig. 6(c) is a magnification of the density distributions in the radial range from 4.5 fm to 6.5 fm.

The lines presented with the experimental observables for p-^{208}Pb in Figs. 6(a) and 6(b), are the medium-modified RIA calculations with the best-fit neutron density (solid), the 3pG neutron density (dash-dotted), and the DH nucleon density (dashed). Although there seems to be little difference between the medium-modified RIA calculations with the best-fit and 3pG neutron density since the solid line overlaps with the dash-dotted line extensively, χ^2 for the 3pG neutron density (=255.3) is about 5σ (=$5\Delta\chi^2 \simeq 55$) larger than $\chi^2_{\rm min}$ (=192.5) especially at data points of high momentum transfer. The difference also appears in the rms radii. Our analysis gave a neutron rms radius for ^{208}Pb of $r_n = 5.653^{+0.026}_{-0.029}$ fm, which is 0.06 fm larger than the value of $r_n = 5.593$ fm of the 3pG neutron density. This means that the data even at high-momentum transfers can affect the rms radius.

In addition to the experimental uncertainty, we evaluated the error envelopes including the model uncertainties in the medium-modified RIA. If the theoretical model was ideal, the reduced $\chi^2_{\rm min}$ should be nearly equal to 1. However, the value of $\chi^2_{\rm min}/\nu$ in this case is about 4, which is far from 1 and shows the incompleteness of this medium-modified RIA model as well as the unknown systematic errors of the experiment. To incorporate this incompleteness into Eq. (6) as the model uncertainties, we simply multiplied the experimental errors by a constant factor S which realizes $\chi^2_{\rm min}/\nu = 1$. Therefore, we defined a new chi-square as $\tilde{\chi}^2 \equiv \chi^2/S^2$ assuming that $\tilde{\chi}^2$

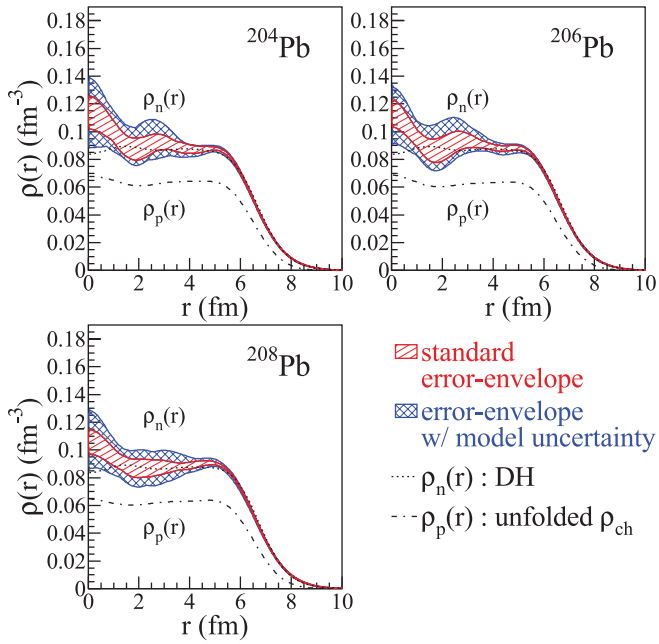

FIG. 7. (Color online) Extracted neutron densities for ^{204,206,208}Pb with two types of error envelopes shown together with DH neutron densities (dotted lines) and point proton densities by unfolding charge densities (dash-dotted lines). The cross-hatched and hatched error envelopes were estimated by Eqs. (8) and (6), respectively.

follows the same χ^2 distribution and Eq. (6)

$$\tilde{\chi}^2 \leqslant \tilde{\chi}^2_{\min} + \Delta\tilde{\chi}^2, \tag{7}$$

where $\tilde{\chi}^2_{\min}/\nu \equiv (\chi^2_{\min}/S^2)/\nu = 1$ and $\Delta\tilde{\chi}^2 = \Delta\chi^2$. Thus Eq. (7) is equivalent to

$$\chi^2 \leqslant \chi^2_{\min} + \Delta\chi^2 \times S^2 = \chi^2_{\min} + \Delta\chi^2 \times (\chi^2_{\min}/\nu). \tag{8}$$

The error envelopes including the model uncertainties were estimated by Eq. (8) for ^{204,206,208}Pb data [42], where $\Delta\chi^2$ for the ^{204,206,208}Pb data is defined as the number of fitted parameters m, namely 11. The cross-hatched areas in Fig. 7 show the error envelopes of the neutron density distributions for ^{204,206,208}Pb obtained from Eq. (8) and the hatched areas are the standard error envelopes due to Eq. (6).

In this analysis for lead isotopes, we neglected the density dependence of ρ and π mesons in the medium modification because the difference between the proton and neutron density is about 1/5 less than the normal density and the modification for ρ and π mesons is expected to be much smaller than for σ and ω mesons. The error from this assumption is also included in the model uncertainties described by Eq. (8). When using a model-dependent hadronic process, it is important to show these error envelopes including the model uncertainties, in parallel with the conventional method of showing the experimental uncertainties only.

Table III lists the best-fit values of the SOG parameters Q_i and $\chi^2_{\min}/\nu$ for each lead isotope. In addition, a fit to the upper and lower error envelopes including the model uncertainties for each isotope was made by using the SOG parameters Q_i of Eq. (5) with the same γ, N, and R_i as used in the investigation of the neutron densities. In this case the normalization condition is not satisfied ($\sum Q_i \neq 1$) because the envelope is not the density distribution itself. The fitted parameters Q_i are listed in Table IV.

TABLE III. Best-fit SOG parameters of the neutron density distributions for ^{204,206,208}Pb. The width γ ($=1.70/\sqrt{3/2}$) and position R_i of the ith Gaussian in Eq. (5) are fixed to the values of the charge distribution [6]. The number in the parentheses are the $\chi^2_{\min}$ over the degrees of freedom ν for each isotope.

i	R_i (fm)	Q_i (the fraction of N in ith Gaussian, $\sum_i Q_i = 1$)		
		^{204}Pb (180.1/47)	^{206}Pb (185.3/47)	^{208}Pb (192.5/47)
1	0.1	0.006 596 1	0.006 889 9	0.005 354 9
2	0.7	0.012 602 3	0.012 320 1	0.010 603 8
3	1.6	0.006 348 9	0.000 002 1	0.020 871 5
4	2.1	0.032 321 2	0.023 171 7	0.009 611 7
5	2.7	0.070 316 1	0.099 854 3	0.076 718 9
6	3.5	0.115 004 1	0.067 759 5	0.063 953 0
7	4.2	0.041 385 4	0.096 108 6	0.132 436 8
8	5.1	0.331 751 8	0.286 032 4	0.248 449 5
9	6.0	0.299 476 8	0.324 954 0	0.346 753 3
10	6.6	0.031 521 7	0.033 325 2	0.027 119 9
11	7.6	0.052 661 4	0.049 582 1	0.058 113 0
12	8.7	0.000 014 2	0.000 000 1	0.000 013 7

E. Neutron rms radii and skin thicknesses

The differences between the rms radius of the best-fit neutron density and the maximum and minimum rms radii in all the neutron densities constituting each error envelope are listed in Table V as the upper and lower errors of the rms radius of neutron $\delta r_n^{\rm mdl}$, with $\delta r_n^{\rm std}$ from Eq. (6). It is found that the effect of the model uncertainty on the errors of r_n for lead isotopes is as large as that of the experimental uncertainty. The neutron rms radii r_n were determined with a good accuracy of about 1% ($\simeq$0.06 fm) even including the model uncertainty.

The systematic behavior of the extracted neutron skin thicknesses Δr_{np} for lead isotopes with the two types of error bars due to $\delta r_n^{\rm std}$ and $\delta r_n^{\rm mdl}$ is shown with previous experimental and theoretical results [13,18,43–47], in Fig. 8. The present result shows a slight increase of the neutron skin thickness at ^{208}Pb. As seen in Fig. 8, the resulting values of the neutron skin thicknesses have similar values and tendency to other results except for the case of NL3 parametrization [45]. The two relativistic models with DD-ME2 and FSUGold parametrization are particularly consistent with our result.

The obtained neutron skin thickness Δr_{np} for ^{208}Pb is compared with those obtained from previous experiments and theoretical models in Table VI. The listed experimental results including this work are not very different within the error bars. In Table VI we list the typical nonrelativistic Skyrme-Hartree-Fock model with SkM* [43] and SkX [49] parametrization. Several relativistic mean field models with NL3 [45], DD-ME2 [46], and FSUGold [47] parametrization

TABLE IV. Fitted SOG parameters Q_i of the upper and lower error envelopes of the neutron density distribution for each lead isotope. γ, N, and R_i are the same as in Table III, but the normalization condition is not satisfied in the case of the envelopes ($\sum Q_i \neq 1$).

i	R_i (fm)	Q_i					
		^{204}Pb		^{206}Pb		^{208}Pb	
		upper	lower	upper	lower	upper	lower
1	0.1	0.009 468 8	0.000 001 6	0.014 027 5	0.000 122 7	0.008 476 8	0.000 129 2
2	0.7	0.012 764 7	0.018 955 6	0.000 767 8	0.015 513 1	0.009 671 9	0.017 256 2
3	1.6	0.000 059 8	0.014 077 7	0.000 003 5	0.000 393 6	0.013 254 2	0.015 742 5
4	2.1	0.031 187 9	0.006 374 8	0.070 476 9	0.004 632 6	0.028 044 0	0.000 087 7
5	2.7	0.145 576 0	0.059 554 9	0.086 465 2	0.062 461 2	0.085 035 4	0.072 394 6
6	3.5	0.008 087 5	0.139 696 2	0.039 842 1	0.090 942 0	0.076 442 2	0.051 604 9
7	4.2	0.139 414 0	0.001 907 1	0.151 639 3	0.022 570 7	0.124 397 3	0.141 671 1
8	5.1	0.284 311 0	0.353 469 1	0.247 764 0	0.227 317 2	0.260 787 3	0.229 630 2
9	6.0	0.339 661 0	0.267 744 0	0.358 047 1	0.241 556 3	0.354 038 1	0.343 433 1
10	6.6	0.018 130 3	0.046 450 1	0.023 135 5	0.021 632 6	0.024 505 4	0.0257194
11	7.6	0.059 342 8	0.045 261 8	0.056 652 6	0.033 057 6	0.066 303 3	0.050 261 0
12	8.7	0.000 022 4	0.000 009 3	0.000 001 8	0.000 002 8	0.000 009 5	0.000 009 5

are also shown. Previously, predictions of the neutron skin thicknesses widely differed between the nonrelativistic and relativistic mean-field models, but recent studies using newly developed relativistic parametrizations such as DD-ME2 and FSUGold have reported Δr_{np} results closer to those of nonrelativistic models than the relativistic model with NL3 parametrization. In the case of FSUGold parametrization, two additional coupling constants that represent nonlinear vector and isoscalar-isovector couplings were introduced based on relativistic effective field theory [50]. The new relativistic parametrization was calibrated to explain the measurements of the giant monopole resonance in ^{90}Zr and ^{208}Pb and the isovector giant dipole resonance in ^{208}Pb, without compromising the quality of the other ground-state properties such as the binding energy per nucleon and the charge radii. The predicted value of $\Delta r_{np} = 0.21$ fm for ^{208}Pb by FSUGold parametrization is in close agreement with our result.

The most recent theoretical studies [51–53], which are constrained by recent experimental data, namely, the x-ray cascade of antiprotonic atoms [18], isospin diffusion in heavy-ion collisions, and pigmy dipole resonance (PDR) data [19], have reported neutron skin thicknesses of ^{208}Pb of 0.20(4) fm [51], 0.22(4) fm [52], and 0.194(24) fm [53], respectively. These obtained values are in remarkable agreement with ours of $\Delta r_{np} = 0.211^{+0.054}_{-0.063}$ fm.

TABLE V. Root-mean-square radii of the charge r_{ch}, proton $r_p^{\rm unfold}$, and neutron r_n used in this work. The two types of errors for r_n, $\delta r_n^{\rm mdl}$, and $\delta r_n^{\rm std}$, are listed (all in fm).

Nucleus	r_{ch}	$r_p^{\rm unfold}$	r_n	$\delta r_n^{\rm std}$	$\delta r_n^{\rm mdl}$
^{204}Pb	5.479(2)	5.420(2)	5.598	$^{+0.029}_{-0.020}$	$^{+0.047}_{-0.059}$
^{206}Pb	5.490(2)	5.433(2)	5.613	$^{+0.026}_{-0.026}$	$^{+0.048}_{-0.064}$
^{208}Pb	5.503(2)	5.442(2)	5.653	$^{+0.026}_{-0.029}$	$^{+0.054}_{-0.063}$

Correlations between the neutron skin for ^{208}Pb and the symmetry energy coefficients of nuclear matter were also reported by various recent theoretical studies [1–3,52,54]. The nuclear matter incompressibility K_0, the symmetry energy J, and its slope L and curvature $K_{\rm sym}$ at saturation density $\rho_{\rm sat}$ are usually expressed as

$$K_0 = 9\rho_{\rm sat}\left.\frac{d^2E(\rho,0)}{d\rho^2}\right|_{\rho=\rho_{\rm sat}}, \tag{9}$$

$$J = S(\rho_{\rm sat}), \tag{10}$$

$$L = 3\rho_{\rm sat}\left.\frac{dS(\rho)}{d\rho}\right|_{\rho=\rho_{\rm sat}}, \tag{11}$$

$$E(\rho,\delta) = E(\rho,0) + S(\rho)\delta^2 + \mathcal{O}(\delta^4), \tag{12}$$

$$S(\rho) = S(\rho_{\rm sat}) + L\epsilon + \frac{K_{\rm sym}}{2}\epsilon^2 + \mathcal{O}(\epsilon^3), \tag{13}$$

where $\rho = \rho_n + \rho_p$ is the total density, $E(\rho,\delta)$ is the energy per nucleon at a density ρ, and a local asymmetry $\delta = (\rho_n - \rho_p)/\rho$. The so-called symmetry energy $S(\rho)$ is expanded around the saturation density [$\epsilon = (\rho - \rho_{\rm sat})/3\rho_{\rm sat}$]. The contributions of the higher-order terms in Eqs. (12) and (13) are negligible at subnormal densities. The incompressibility K_0 is now expected to be about 210–250 MeV [46,47,55,56] constrained by many measurements of isoscalar giant resonances for various nuclei [57–59]. The symmetry energy J at saturation is also known to be ~32 MeV, but L and $K_{\rm sym}$ are still less certain and their predicted values vary widely among many theoretical models. Particularly the slope coefficient L of the symmetry energy at saturation density is strongly correlated with Δr_{np} for ^{208}Pb [52,54]. Our results support a value of $L \sim 60$ MeV predicted by FSUGold parametrization, which is consistent with $L = 88 \pm 25$ MeV obtained from the analysis of isospin diffusion data [52] and $L = 65 \pm 16$ MeV determined by the energy-weighted sum rule of PDR data [53]. However, the uncertainty of Δr_{np} is still so large that the constraint on the slope coefficient L is

TABLE VI. Obtained values of r_n, r_p, and Δr_{np} for ^{208}Pb compared with several experimental and theoretical results (all in fm). Except for this work, the errors are statistical only.

	Model					Experiment					
	SkM*	SkX	NL3	DD-ME2	FSUGold	GDR[a]	PDR[b]	antiproton[c]	(p, p) at 800 MeV[d]	(p, p) at 650 MeV[e]	This work
r_p	5.45	5.44	5.46	–	–	–	–	5.44	5.45	5.46	5.442(2)
r_n	5.62	5.60	5.74	–	–	–	–	5.60	5.59(4)	5.66(4)	$5.653^{+0.054}_{-0.063}$
Δr_{np}	0.17	0.16	0.28	0.19	0.21	0.19(9)	0.18(4)	0.16(2)	0.14(4)	0.20(4)	$0.211^{+0.054}_{-0.063}$

[a]The isovector giant dipole resonance (GDR) from ^{208}Pb(α, α') at $E_\alpha = 120$ MeV [12].
[b]The measurement of "pigmy" dipole resonance (PDR) strength from ^{208}Pb(γ, γ') [19].
[c]The analysis of the x-ray cascade from antiprotonic atoms assuming two-parameter-Fermi distribution for both ρ_p and ρ_n [18].
[d]Ref. [9].
[e]Ref. [13].

30–90 MeV, roughly estimated by the correlation in Ref. [54]. Thus we need to develop our analysis and experimental data for a more precise measurement of the neutron skin thickness. Extending our analysis to other nuclei is also important to improve the constraint on the value of the slope L.

IV. SUMMARY

We measured the angular distributions of cross sections and analyzing powers for polarized proton elastic scattering from ^{58}Ni and ^{204,206,208}Pb at $E_p = 295$ MeV. Using the experimental data, we extracted the neutron density distributions of ^{204,206,208}Pb. To explain the proton elastic scattering at intermediate energies, phenomenological medium modifications were introduced into the free NN interaction with density-dependent parameters. The medium-effect parameters were determined from the experimental observables for ^{58}Ni, whose nucleon density is well known. After the calibration of the effective NN interaction, we deduced the neutron density distributions of ^{204,206,208}Pb in the form of a model-independent SOG distribution.

Furthermore, we evaluated the error envelopes of the neutron densities due to both experimental uncertainties and uncertainties associated with the various model assumptions in the medium-modified RIA by means of a new χ^2 criterion. The rms radius of the neutron density for ^{208}Pb is consistent with past results and recent theoretical predictions such as FSUGold parametrization. The experimental standard errors of the neutron rms radii ($\delta r_n^{\rm std} \simeq 0.03$ fm) are slightly smaller than the value of Ref. [13]. Even including the model ambiguity, the estimated errors of the neutron rms radii ($\delta r_n^{\rm mdl} \simeq 0.06$ fm) were found to be relatively small with an accuracy of about 1%, but not so small as to determine the slope coefficient L of the nuclear symmetry energy at saturation density.

Since unknown systematic errors are also included in the model uncertainties, further progress from both the experiment and theory are necessary.

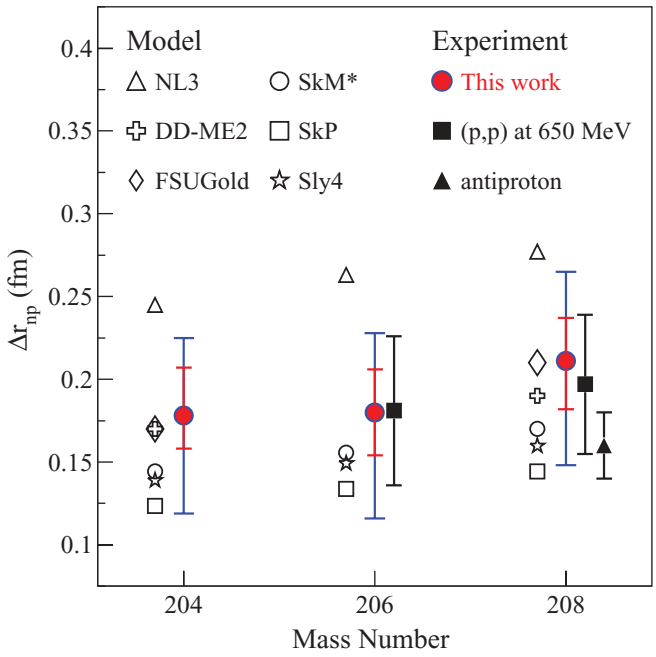

FIG. 8. (Color online) Systematic behavior of the neutron skin thicknesses for ^{204,206,208}Pb. The filled circles are the results of this work with the two types of error bars. The filled squares and triangle are from the analysis of proton elastic scattering at 650 MeV [13] and x rays from antiprotonic atoms [18], respectively, with statistical errors only. The open triangles, crosses, and diamonds show the calculations of relativistic mean-field models with NL3 [45], DD-ME2 [46], and FSUGold [47] parametrization and the open circles, squares, and stars are from nonrelativistic mean-field models with SkM* [43], SkP [44], and Sly4 [48] parametrization.

ACKNOWLEDGMENTS

The authors would like to express our gratitude to K. Hatanaka and the RCNP crew for their continuing support in providing the stable beam. The authors would like to thank A. Tamii, T. Kawabata, and the late H. Okamura for their support and helpful discussions regarding this work. This experiment was performed under Program No. E248 at RCNP. Some of the authors (J. Z. and S. T.) acknowledge support from the Japan Society for the Promotion of Science (JSPS).

[1] B. A. Brown, Phys. Rev. Lett. **85**, 5296 (2000).
[2] R. J. Furnstahl, Nucl. Phys. A **706**, 85 (2002).
[3] S. Yoshida and H. Sagawa, Phys. Rev. C **69**, 024318 (2004); **73**, 044320 (2006).
[4] C. J. Horowitz and J. Piekarewicz, Phys. Rev. Lett. **86**, 5647 (2001).
[5] C. J. Horowitz and J. Piekarewicz, Phys. Rev. C **66**, 055803 (2002).
[6] H. de Vries, C. W. de Jager, and C. de Vries, At. Data Nucl. Data Tables **36**, 495 (1987).
[7] I. Angeli, At. Data Nucl. Data Tables **87**, 185 (2004).
[8] R. R. Johnson *et al.*, Phys. Rev. Lett. **43**, 844 (1979).
[9] L. Ray, W. R. Coker, and G. W. Hoffmann, Phys. Rev. C **18**, 2641 (1978); L. Ray, *ibid.* **19**, 1855 (1979); G. W. Hoffmann *et al.*, *ibid.* **21**, 1488 (1980).
[10] H. J. Gils, H. Rebel, and E. Friedman, Phys. Rev. C **29**, 1295 (1984).
[11] B. M. Barnett *et al.*, Phys. Lett. B **156**, 172 (1985).
[12] A. Krasznahorkay *et al.*, Nucl. Phys. A **567**, 521 (1994).
[13] V. E. Starodubsky and N. M. Hintz, Phys. Rev. C **49**, 2118 (1994).
[14] S. Karataglidis, K. Amos, B. A. Brown, and P. K. Deb, Phys. Rev. C **65**, 044306 (2002).
[15] B. C. Clark, L. J. Kerr, and S. Hama, Phys. Rev. C **67**, 054605 (2003).
[16] A. Krasznahorkay *et al.*, Nucl. Phys. A **731**, 224 (2004).
[17] A. Trzcińska, J. Jastrzebski, P. Lubiński, F. J. Hartmann, R. Schmidt, T. von Egidy, and B. Kłos, Phys. Rev. Lett. **87**, 082501 (2001).
[18] B. Kłos *et al.*, Phys. Rev. C **76**, 014311 (2007).
[19] A. Klimkiewicz *et al.*, Phys. Rev. C **76**, 051603(R) (2007).
[20] H. Sakaguchi *et al.*, Phys. Rev. C **57**, 1749 (1998).
[21] S. Terashima *et al.*, Phys. Rev. C **77**, 024317 (2008).
[22] F. Hofmann, C. M. Keil, and H. Lenske, Phys. Rev. C **64**, 034314 (2001).
[23] A. N. Antonov *et al.*, Phys. Rev. C **72**, 044307 (2005).
[24] T. W. Donnelly, J. Dubach, and Ingo Sick, Nucl. Phys. A **503**, 589 (1989).
[25] C. J. Horowitz, S. J. Pollock, P. A. Souder, and R. Michaels, Phys. Rev. C **63**, 025501 (2001).
[26] R. Michaels *et al.*, Proposal to Jefferson Laboratory, PAC 29 (2005).
[27] K. Hatanaka *et al.*, Nucl. Instrum. Methods Phys. Res. A **384**, 575 (1997).
[28] T. Ichihara, H. Sakaguchi, K. Hatanaka, M. Fujiwara, and K. Hosono, RCNP Annual Report 1981, p. 194.
[29] M. Fujiwara *et al.*, Nucl. Instrum. Methods Phys. Res. A **422**, 484 (1999).
[30] H. Takeda, Memoirs of the Faculty of Science, Kyoto University, Series of Physics, Astrophysics, Geophysics and Chemistry, Vol. XXXXIV, No. 1, Article 1, 2003.
[31] N. Fujita *et al.*, RCNP Annual Report 2008, Sec. 1, p. 2.
[32] D. P. Murdock and C. J. Horowitz, Phys. Rev. C **35**, 1442 (1987); C. J. Horowitz, D. P. Murdock, and B. D. Serot, *Computational Nuclear Physics 1* (Springer-Verlag, Berlin, 1991), Chap. 7.
[33] E. D. Cooper, S. Hama, and B. C. Clark, Phys. Rev. C **80**, 034605 (2009).
[34] C. J. Horowitz and B. D. Serot, Nucl. Phys. A **368**, 503 (1981).
[35] I. Sick, Nucl. Phys. A **218**, 509 (1974); B. Frois, J. B. Bellicard, J. M. Cavedon, M. Huet, P. Leconte, P. Ludeau, A. Nakada, P. Z. Ho, and I. Sick, Phys. Rev. Lett. **38**, 152 (1977).
[36] W. Bertozzi, J. Friar, J. Heisenberg, and J. W. Negele, Phys. Lett. B **41**, 408 (1972).
[37] I. Sick, Phys. Lett. B **576**, 62 (2003); P. G. Blunden and I. Sick, Phys. Rev. C **72**, 057601 (2005).
[38] J. Arrington and I. Sick, Phys. Rev. C **76**, 035201 (2007).
[39] J. J. Kelly, Phys. Rev. C **70**, 068202 (2004).
[40] K. Melnikov and T. van Ritbergen, Phys. Rev. Lett. **84**, 1673 (2000).
[41] P. R. Bevington and D. K. Robinson, *Data Reduction and Error Analysis for the Physical Science*, 3rd edition (McGraw-Hill, New York, 2003).
[42] In Ref. [21] it was reported that the error envelopes of tin isotopes were estimated by Eq. (8) for the neutron-density parameters together with Eq. (6) for the medium-effect parameters, simultaneously. In that case, however, the envelope is doubly estimated because the fluctuation of the medium-effect parameters indicated by Eq. (6) is a part of the uncertainty associated with the various model assumptions described by Eq. (8). Thus, Eq. (8) is sufficient to evaluate the error envelopes including the model uncertainties.
[43] J. Bartel, P. Quentin, M. Brack, C. Guet, and H.-B. Håkansson, Nucl. Phys. A **386**, 79 (1982).
[44] J. Dobaczewski, H. Flocard, and J. Treiner, Nucl. Phys. A **422**, 103 (1984).
[45] G. A. Lalazissis, J. König, and P. Ring, Phys. Rev. C **55**, 540 (1997); G. A. Lalazissis, S. Raman, and P. Ring, At. Data Nucl. Data Tables **71**, 1 (1999).
[46] G. A. Lalazissis, T. Nikšić, D. Vretenar, and P. Ring, Phys. Rev. C **71**, 024312 (2005).
[47] B. G. Todd-Rutel and J. Piekarewicz, Phys. Rev. Lett. **95**, 122501 (2005).
[48] E. Chabanat, P. Bonche, P. Haensel, J. Meyer, and R. Schaeffer, Nucl. Phys. A **635**, 231 (1998).
[49] B. A. Brown, Phys. Rev. C **58**, 220 (1998).
[50] H. Müller and B. D. Serot, Nucl. Phys. A **606**, 508 (1996).
[51] B. A. Brown, G. Shen, G. C. Hillhouse, J. Meng, and A. Trzcińska, Phys. Rev. C **76**, 034305 (2007).
[52] L.-W. Chen, C. M. Ko, and B.-A. Li, Phys. Rev. C **72**, 064309 (2005).
[53] A. Carbone, G. Colò, A. Bracco, L.-G. Cao, P. F. Bortignon, F. Camera, and O. Wieland, Phys. Rev. C **81**, 041301(R) (2010).
[54] M. Centelles, X. Roca-Maza, X. Viñas, and M. Warda, Phys. Rev. Lett. **102**, 122502 (2009); M. Warda, X. Viñas, X. Roca-Maza, and M. Centelles, Phys. Rev. C **80**, 024316 (2009).
[55] R. Kumar, B. K. Agrawal, and S. K. Dhiman, Phys. Rev. C **74**, 034323 (2006).
[56] B. K. Agrawal, Phys. Rev. C **81**, 034323 (2010).
[57] M. Itoh *et al.*, Phys. Lett. B **549**, 58 (2002); Phys. Rev. C **68**, 064602 (2003).
[58] M. Uchida *et al.*, Phys. Lett. B **557**, 12 (2003); Phys. Rev. C **69**, 051301(R) (2004).
[59] T. Li *et al.*, Phys. Rev. C **81**, 034309 (2010).